Check for updates

# Covalency competition dominates the water oxidation structure–activity relationship on spinel oxides

Yuanmiao Sun[1,13], Hanbin Liao[1,2,13], Jiarui Wang[1,3], Bo Chen[1], Shengnan Sun[1,11], Samuel Jun Hoong Ong[1,3], Shibo Xi[4], Caozheng Diao[5], Yonghua Du[4,12], Jia-Ou Wang[6], Mark B. H. Breese[5], Shuzhou Li[1], Hua Zhang[7,8] and Zhichuan J. Xu[1,9,10] ✉

**Spinel oxides have attracted growing interest over the years for catalysing the oxygen evolution reaction (OER) due to their efficiency and cost-effectiveness, but fundamental understanding of their structure–property relationships remains elusive. Here we demonstrate that the OER activity on spinel oxides is intrinsically dominated by the covalency competition between tetrahedral and octahedral sites. The competition fabricates an asymmetric $M_T$—O—$M_O$ backbone where the bond with weaker metal–oxygen covalency determines the exposure of cation sites and therefore the activity. Driven by this finding, a dataset with more than 300 spinel oxides is computed and used to train a machine-learning model for screening the covalency competition in spinel oxides, with a mean absolute error of 0.05 eV. $[Mn]_T[Al_{0.5}Mn_{1.5}]_OO_4$ is predicted to be a highly active OER catalyst and subsequent experimental results confirm its superior activity. This work sets mechanistic principles of spinel oxides for water oxidation, which may be extendable to other applications.**

The rise in global energy consumption brings increasing demand for the development of a sustainable and clean energy infrastructure[1,2]. Hydrogen gas, which can be produced from water electrocatalysis, is considered an ideal energy carrier due to its high energy density and cleanliness[3]. However, water splitting suffers overall from a sluggish oxygen evolution reaction (OER) at the anode, which makes the development of an efficient OER catalyst a critical effort[4,5]. Ideally, remarkable OER catalyst should fulfil the requirements as both catalytically active and economically feasible[6–8]. Transition metal spinel oxides ($AB_2O_4$), where $A^{2+}$ and $B^{3+}$ cations occupy the tetrahedral and octahedral sites, respectively, have attracted substantial attention due to their abundance and cost-effectiveness[9–11]. Tremendous efforts have been spent raising the OER activity of spinel oxides. For example, substituting some cobalt with iron in $ZnCo_2O_4$ ($ZnFe_xCo_{2-x}O_4$) is found to promote the OER activity over $ZnCo_2O_4$, as the injection/extraction of electrons from oxygen is facilitated by iron substitutes[12]. Duan et al. have incorporated nickel and cobalt into the octahedral sites of the spinel; the constructed $ZnNi_xCo_{2-x}O_4$ ($x = 0.6, 0.8$) possesses activated lattice oxygen, which gives rise to continuously formed oxyhydroxide as surface-active species and thus enhanced activity[13]. Despite several successful attempts, the reported strategies so far only apply to respective and narrow groups of spinel oxides. A universal principle is required to promote a more rational screen

and design of effective spinel oxide OER catalysts because of their broad compositional diversity. A fundamental understanding that elucidates the structure–property relationship of the OER on spinel oxides is essential and critical for establishing such a principle.

A well-defined structure–property relationship of OER on transition metal oxides (TMOs) has been established by Grimaud and colleagues, where the activity of perovskite oxides is described by the bulk oxygen $2p$ band centre[14]. This finding highlights the rationality of bridging the OER activity of TMOs with their bulk thermochemistry. More recent studies on the lattice-oxygen-participated mechanism (LOM) of the OER on perovskites has demonstrated the dominance of the bulk metal–oxygen covalency of $TMO_6$ in determining the reaction kinetics[15]. This provides valuable clues in designing excellent OER catalysts from spinel oxides as they also contain the $TMO_6$ structural unit as the perovskite oxides do. However, as the $AB_2O_4$ frame of the spinel enables both A and B sites to be resided by transition metals, the co-existence of $TMO_4$ and $TMO_6$ produces more challenges in establishing an accurate structure–property relationship.

In this work we employ both computational and experimental methods to demonstrate the dominant role of the covalency competition between tetrahedral and octahedral sites in determining the OER activity of spinel oxides. After analysing dozens of reported spinels, a volcano plot bridging the OER activity and bulk

structural parameter is established. Furthermore, we compute and generate a dataset of more than 300 spinels that forms the basis from which a machine-leaning assisted approach is employed for ultra-fast and accurate covalency prediction. Our machine-leaning model shows only 0.05 eV mean absolute error for screening the covalency competition in spinels. Using this approach, a spinel oxide with outstanding OER activity has been designed and its activity is confirmed by subsequent experiments. Our findings elucidate a comprehensive structure–property relationship of the OER on spinel oxides. The electronic database and the machine-learning model developed here may be extendable for developing spinel oxides for other applications.

## Results

**Relationship between structural properties and the reaction mechanism.** Bulk spinel oxide exhibits an $Fd3m$ space group, with each oxygen atom connected to one tetrahedral cation and three octahedral cations (Fig. 1a). Within the structure, tetragonal and octahedral cations are surrounded by four and six negatively charged oxygens, respectively, which produce a repulsive force to the electrons of the cations. This repulsive effect, known as the Madelung potential, is determined by crystallography and is evaluated by summing the electrostatic interactions $q^2/r$, where $q$ and $r$ represent the charge and interatomic distance, respectively[16]. Conversely, the electronic energy of oxygen anions is stabilized by the surrounding positively charged metal cations. Due to the crystal field effect, the static electric field splits the $d$ orbitals of the tetrahedral cation into two low-lying $e$ orbitals and three high-lying $t_2$ orbitals, whereas the $d$ orbitals of the octahedral cation are split into three low-lying $t_{2g}$ orbitals and two high-lying $e_g$ orbitals (Supplementary Fig. 1). The split $d$ orbitals in each cation together contribute to the narrow $d$ band, which ionically or covalently interacts with the broad oxygen $p$ band, giving the spinel oxide structure[17]. Specifically, both metals in the tetrahedral and octahedral sites have electrons that spatially overlap with the oxygen orbitals, forming $\sigma$- and $\pi$-bonding molecular orbital (MO) states and antibonding MO* states. Moreover, as three metal cations (each having five $d$ orbitals) and four oxygens (each having three $2p$ orbitals) are incorporated into spinel $AB_2O_4$, some oxygen orbitals may not hybridize with metallic states, depending on the symmetry or components of the structure (that is, when lithium, aluminium or magnesium is contained), instead forming non-bonding and purely oxygen $p$ states (Fig. 1b). These states constitute an extended three-dimensional crystal band that can be integrated to obtain a density of states (DOS) diagram that represents the electronic density for each state in a projective view.

The OER can occur via two distinct mechanisms, the adsorbate evolution mechanism (AEM) or the LOM[18]. In the former, the reactant (OH⁻) donates electrons at the anode surface and evolves to generate oxygen gas via *OH, *O, *OOH and * (or *OO) intermediates bound to the surface active sites, whereas in the latter, lattice oxygen participates in the reaction cycle and becomes part of the gaseous products (Supplementary Fig. 2). To be involved in the OER cycle, the lattice oxygen must be active enough to escape and segregate from the lattice and interact with the adsorbed oxygen (*O), which is generated elsewhere during the cycle, leaving a ligand hole (vacancy) in the lattice that becomes a new active site.

However, as bias exists, intralattice charge transfer occurs during the electrochemical process, which could lead to local charge redistribution[19]. Energetically, in terms of the relative position between oxygen and metal cations, two possible conditions exist in bulk spinel. When oxygen exhibits a lower energy level than metal cations (tetrahedral or octahedral), electrons transfer from metal cations to oxygen during the electrochemical reaction, which constrains the oxygen inside the lattice and blocks the escape and segregation of the lattice oxygen. However, when the band centre of oxygen lies above both cations, the closer position of the oxygen $2p$ band centre

relative to the Fermi level might force the electron flow from oxygen to nearby cations, which reduces the charges on oxygen. The reduced oxygen has higher degrees of freedom and is thus easily released from the lattice. Both the absolute energy level of the bulk oxygen $p$ band, and the relative energy level between the oxygen $p$ band and metal $d$ band, should therefore be evaluated to define the reaction mechanism from the electronic point of view. Figure 1c illustrates the calculated oxygen $2p$ band centre and the energy difference between the oxygen $2p$ and metal $3d$ band centres (here the metal represents the more active one between octahedral and tetrahedral cations) in more than thirty spinel oxides whose OER reaction mechanisms have been investigated[12,13,20]. As illustrated, spinels exhibiting the LOM and AEM mechanisms are in the top-right and bottom-left domains, respectively, suggesting two distinguishable energetical features. The lattice oxygens in the LOM spinels satisfy both the activity and priority criteria; that is, the oxygen $2p$ band centre is high enough (greater than −1.75 eV) to guarantee its escape from the lattice, and the oxygen $p$ band level is higher than both cations, which results in intramolecular charge transfer from oxygen to cations and reduces the charge on oxygen. The oxygen $p$ band centre and the relative centre between the oxygen $p$ band and metal $d$ band thus concurrently regulate the reaction mechanism of the OER. Making full use of the dual-parameter, the reaction mechanism of OER on a given spinel oxide can be effectively foreseen. Meanwhile, we believe this dual-parameter can be also used to predict spinel oxides that are not stable and exhibit phase separation, which will need sufficient experimental validations in future.

**Covalency competition between tetrahedral and octahedral sites.** In the $AB_2O_4$ spinel framework, cations in both the tetrahedral and octahedral sites can be covalently bound to oxygen anions (Fig. 2a). The two types of bond formed, $M_T$−O and $M_O$−O, are a result of the orbital overlap between the metal $d$ orbitals (or $p$ orbitals, for example, for aluminium and magnesium) and oxygen $p$ orbitals[17]. As each oxygen is shared by both tetrahedral and octahedral cations, covalency competition exists between the tetrahedral and octahedral cations for overlapping with the full oxygen $p$ orbitals (denoted as $M_T$−$M_O$ competition), resulting in an asymmetrical $M_T$−O−$M_O$ backbone, in which either $M_T$−O or $M_O$−O is weaker. Under OER conditions, where bias exists, the surface structural rearrangement of spinel oxides may occur and bond breakage is much more likely to be at the weaker bond in the $M_T$−O−$M_O$ backbone. In this process, the weaker bond (either $M_T$−O or $M_O$−O) breaks, dividing the $M_T$−O−$M_O$ backbone into two counterparts, M−O and M−. The cations in M−O are still fully coordinated and thus rarely contribute to the reaction performance. The barely exposed metals (M−), if having unpaired valence electrons, should serve as active sites to adsorb one solvated OH⁻, generating M−OH species (Fig. 2a) to start an OER cycle; that is, the breakage of either $M_T$−O or $M_O$−O in the $M_T$−O−$M_O$ backbone can create exposed metal sites that can become involved in the reaction cycle.

As commencing the OER requires metal cations on the surface to react with hydroxyl groups, creating exposed cations is important for promoting the performance of a catalyst[21]. We may hypothesize that the difficulty in breaking the M−O bond of a spinel, which gives rise to exposed metal sites that can immediately take part in the OER cycle, is directly correlated to its initial reaction performance (at low overpotential or current). To quantitatively describe the possibility of breaking the M−O bond, the covalency obtained from the projected DOS is used to correlate the experimentally observed OER activity (potential (versus RHE) at 25 µA cm$_{ox}^{-2}$). The covalency is quantified by the distance between the centres of the metal $d$ and oxygen $p$ bands (denoted as $D_M$, in units of electronvolts). A higher value of $D_M$ indicates a weaker M−O covalency and thus easier bond breakage for the creation of active sites. In spinels, M−O breakage occurs at the bond that exhibits a weaker M−O covalency in the
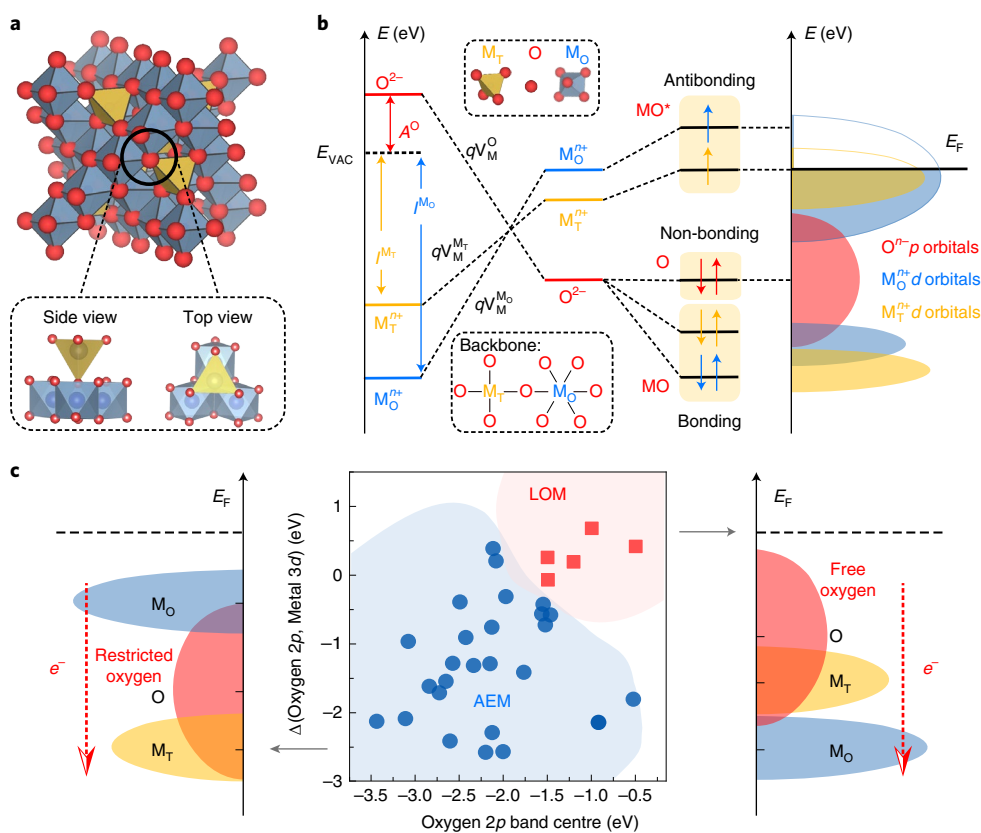
**Fig. 1 | Patterning OER mechanisms on spinel oxides based on the DOS. a**, The crystal structure of spinel oxide. The polyhedra in orange and blue represent cations in tetrahedral and octahedral sites, respectively. The red atoms depict oxygen anions. The lower box illustrates the side and top views of the primitive spinel unit, in which one tetrahedral cation and three octahedral cations are connected to one oxygen anion. **b**, The formation of a density of states (DOS) diagram for spinel oxide with the contributions from tetragonal cations ($M_T$), octahedral cations ($M_O$) and oxygen anions (O). The formation originates from the ionization energy of metal cations ($I^M$) as well as the electron affinity of oxygen ($A^O$). $q$ and $V$ represent the charge and Madelung potential, respectively. The crystal interaction gives rise to antibonding MO* states, purely oxygen non-bonding oxygen states and bonding MO orbitals, which compose an extended 3D crystal band that can be integrated to obtain a DOS diagram, representing the electronic density for each state in a projective view. **c**, An illustration of how the oxygen 2$p$ band centre, and the relative band centres between oxygen 2$p$ and active metal 3$d$, co-regulate the reaction mechanism of OER on spinel oxides. For spinels where the energy level of the oxygen $p$ band centre is low or oxygen is less active than the metal cations, the lattice oxygen is firmly restricted and the AEM dominates. For spinels whose oxygen $p$ band centre is high (for example, greater than −1.75 eV) and higher than or close to the cation $d$ band centre, the lattice oxygen has a higher degree of freedom and the LOM is likely to occur. The experimental reaction mechanisms are referenced from reported works[12,13,20] and unpublished works (Supplementary Table 1). The band centres of spinel oxides are calculated through DFT calculations (Supplementary Table 1).

$M_O$−O−$M_T$ backbone, the higher $D_M$ between $D_T$ and $D_O$ (denoted as $Max(D_T, D_O)$, where $D_T$ and $D_O$ represent the covalency between tetrahedral/octahedral cations and oxygen, respectively) is therefore used to correlate the OER activity (potential at 25 µA $cm_{ox}^{-2}$).

After analysing dozens of reported spinel oxides[12,13,20], we plotted their OER activity as a function of their calculated $Max(D_T, D_O)$, which displays a volcano-like shape (Fig. 2c). Spinel oxides on the very left side of the volcano graph exhibit strong covalency for both types of M−O bond, which makes it difficult (or impossible) for them to generate active sites, thus exhibiting low OER activity. Although those at the very right part of the volcano have at least one M−O bond with low covalency, suggesting an easy bond break, the low covalency intrinsically suggests a highly polar chemical bond, where the electrons forming the bond are unequally distributed. In this case, bond breakage will result in formation of two ionic components, which have no unpaired electrons and hence can hardly be active to adsorb hydroxyl groups for the next OER. Alternatively, at the middle part of the volcano, the bond is neither too strong nor too polarized. When bias is applied, the bond is likely to break. Also, as the polarity is not high enough for ion formation, bond breakage will end up with an equal distribution of the shared electron pairs

between metal and oxygen, resulting in metals with unpaired electrons exposed, which can act as actives sites in the reaction cycle and contribute to the OER performance. In other words, to generate active sites, two conditions need to be satisfied. First, the M−O bond should not be too strong, which guarantees bond breakage under electrochemical conditions. Second, the bond should not be too polarized, which enables the formation of exposed metals with unpaired electrons rather than ions. The peak of the volcano is located at around 3 eV, indicating that spinels with a 3 eV value of $Max(D_T, D_O)$ are excellent candidates for catalysing the OER. It is worth mentioning that it is the $AB_2O_4$ framework of spinel oxide that makes the $M_T$−$M_O$ competition crucial in determining the OER activity, as all of the other factors discovered based on perovskite oxides, such as oxygen 2$p$ band centre[14,22], bulk oxygen vacancy formation energy[22], $e_g$ occupation of the $TMO_6$ structural unit[23], and single M−O covalency[15], are not universally applicable to the experimental results for all of the spinel oxides reported so far (Supplementary Fig. 3). In the perovskite $ABO_3$ frame, alkaline or rare-earth metals normally reside in the A sites and their contributions to the OER are relatively insignificant. A rational elucidation of B-site cations, or B−O covalency, is thus sufficient to describe
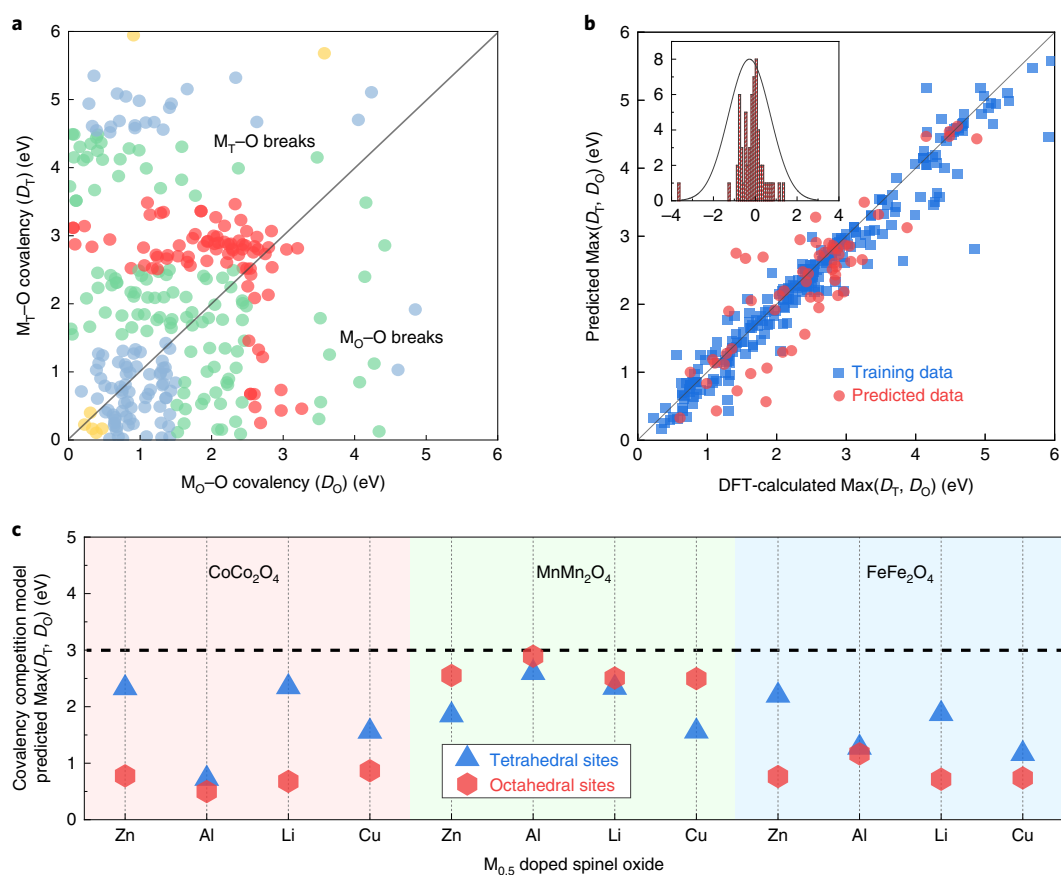
**Fig. 2 | Relationship between OER activity and the covalency competition in spinel oxides. a**, An illustration of how the covalency competition between tetrahedral and octahedral cations in overlapping with oxygen $p$ orbitals ($M_T$–$M_O$ competition) results in an asymmetrical $M_T$–O–$M_O$ backbone, and how the two components generated from M–O bond breakage participate in the reaction cycle. **b**, Three possible bond breakage scenarios according to different metal–oxygen covalencies. For strong M–O covalencies (with a short distance between the metal band centre and oxygen band centre, the pink domain), the bond is difficult to break. For weak M–O covalencies (the blue domain), bond breakage will lead to two (partially) ionic parts due to high polarity. For intermediate M–O covalencies (the green domain), bond breakage will result in the exposure of the metal with free radicals. Note that bond breakage in the spinel structure takes place at the weaker bond in the $M_O$–O–$M_T$ backbone. **c**, The experimentally observed reaction activity as a function of the calculated $Max(D_T, D_O)$ (eV), where $D_T$ represents the distance between the centres of tetrahedral metal $d$ and oxygen $p$ bands, and $D_O$ refers to the distance between the centres of the octahedral metal $d$ and oxygen $p$ bands. The experimental activity is defined as the potential (V versus RHE) at a given specific current density; that is, 25 μA cm$_{ox}^{-2}$ for the OER. All of the experimental data are taken from published papers[12,13,20] and unpublished works. The details including the potential at 25 μA cm$_{ox}^{-2}$ (V versus RHE), the simulated compositions and the calculated $Max(D_T, D_O)$ values are summarized in Supplementary Table 2.

the OER on perovskites. However, the spinel $AB_2O_4$ frame allows transition metals to reside in both A and B sites, which implies that both tetrahedral and octahedral cations could take part in the OER cycle. The chemical features of both A–O and B–O need to be considered to set up a universal design principle. This defines the principal distinction between perovskites and spinels, which ultimately makes the covalency competition between tetrahedral and octahedral sites critical in determining the OER activity. Besides, the covalency competition theory established here may also provide clues to explain the catalytic activity on other types of materials, where multiple catalytic sites exist.

**Machine-learning approach for fast screening the covalency competition.** Although it has been unveiled how the nature of spinel $M_T$–$M_O$ competition determines the OER activity, the summit of the volcano remains vacant. To deeply explore the potential of spinels in oxygen electrocatalysis and find out a benchmark spinel oxide, we calculate and generate a comprehensive dataset with more than 300 spinels, where normal, (partially) inversed, metal

substituted and defective compositions have all been considered. As shown in Fig. 3a, most of the calculated spinels are in the top-left of the panel, indicating that octahedral cations tend to bind oxygen more tightly than tetrahedral cations. Among the screened spinels, only a few with tetrahedral zinc and lithium have a $D_T$ ranging from 4 eV to 6 eV, suggesting the possible utility of these two cations in weakening the metal–oxygen covalency. Plentiful spinel oxides estimate top-class OER activity, as their $Max(D_T, D_O)$ values are close to the optimal level (the red dots). Spinel oxides are therefore theoretically an ideal class of materials for catalysing the OER. As this work utilizes bulk thermochemistry to describe the OER activity, the solvation model that addresses the role of electrolyte to the solid–liquid interface is not included. It is worth noting that the OER activities of some materials are reported to exhibit dependence on the type of cationic species[24–26] and the pH value[12,15] of the electrolyte; however, as the electrolyte's function is to influence the thermodynamics and kinetics at the catalyst–electrolyte interface, although the absolute activity may evolve following a change of electrolyte, the relative trend should remain the same.

**Fig. 3 | Machine-learning approach for fast screening the covalency competition in spinel oxides. a**, The calculated electronic dataset of more than 300 spinel oxides. The x- and y-axes present the $M_O$−O ($D_O$) and $M_T$−O ($D_T$) covalencies, respectively. The red dots represent those with covalencies in the 2.5 eV to 3.5 eV range; the green dots represent those with covalencies in the 1.5 eV to 2.5 eV and 3.5 eV to 4.5 eV ranges; the blue dots represent those with covalencies in the 0.5 eV to 1.5 eV and 4.5 eV to 5.5 eV ranges; and the yellow dots represent those with covalencies in the 0 eV to 0.5 eV and 5.5 eV to 6 eV ranges. Of all of the screened spinels, only those with both $D_T$ and $D_O$ values ranging from 0 eV to 6 eV are shown. A detailed structural composition and the metal–oxygen covalencies of the dataset can be found in Supplementary Tables 3−6. **b**, The established machine-learning model (covalency competition model) for screening the covalency competition in spinel oxides is shown. The x-axis in the inset shows the deviation between the covalency-competition-model-predicted and DFT-calculated $Max(D_T, D_O)$ values, whereas the y-axis represents the counts of the dots. The feature sets are summarized in Supplementary Table 7. **c**, The $Max(D_T, D_O)$ values of $M_{0.5}$-substituted (M = Zn, Al, Li and Cu) $CoCo_2O_4$, $MnMn_2O_4$ and $FeFe_2O_4$ predicted by the covalency competition model. The blue and red dots denote spinel $[M_{0.5}Mn_{0.5}]_T[Mn_2]_OO_4$ and $[Mn]_T[M_{0.5}Mn_{1.5}]_OO_4$, respectively.

After obtaining the dataset, we apply statistical and machine-learning techniques (more details are summarized in the Methods, Supplementary Table 7, and Supplementary Figs. 4 and 5) to screen the covalency competition in spinel oxides[27]. The feature-based approach is employed to make the screening precise and accurate, in which both the elemental and structural features of the spinel are considered. Elementally, the atomic radius, number of valence electrons and cutoff energy for the plane-wave basis are coded to describe anions and cations (the sets are detailed in Supplementary Table 7). Structurally, as two types of cations coexist in the spinel lattice, the tetrahedral and octahedral sites are described individually. In the $AB_2O_4$ lattice, the crystal has the zinc-blende structure if all of the octahedral sites are empty and only the tetrahedral sites are filled, whereas the crystal exhibits the rock-salt structure if only octahedral sites are occupied[17]. To simplify, the spinel lattice may thus be thought of as an ordered mixture of the zinc-blende and rock-salt structures. It is therefore expected that the metal–oxygen covalencies in zinc-blende and rock-salt can be used to describe the structural features of spinels. By considering both the elemental and structural features, a machine-learning model (denoted as the covalency competition model) is established

using the random forest algorithm (Fig. 3b). The machine-learning algorithm was verified by analysing the mean absolute error (MAE), which is only 0.05 eV for the predicted $Max(D_T, D_O)$ values from this model, indicating that the data predicted by the model match closely with those calculated by density functional theory (DFT). By contrast, the MAE from the model in which the data are trained without the structural feature is considerably higher, with a value of 0.09 eV (Supplementary Fig. 6). This provides a direct indication of the mathematical correlation between the covalencies in spinels and those in the zinc-blende and rock-salt structure. When crystallizing a spinel structure, oxygen is no longer bound to a single type of cation, but is shared simultaneously by tetrahedral and octahedral cations. The competition between these two types of cations in overlapping with the oxygen p orbitals exists in the $M_O$−O−$M_T$ backbone, which finally contributes and shapes the whole covalency pattern in spinel oxides. With the covalency competition machine-learning model established, both the reaction mechanism and the covalency competition in spinels can be ultrafast predicted.

Using the covalency competition model, several spinel oxides comprising earth-abundant elements have been screened and their $Max(D_T, D_O)$ values are generated. Specifically, we have used

$M_{0.5}$ (M = Zn, Al, Li and Cu) to substitute the cations in $CoCo_2O_4$, $MnMn_2O_4$ and $FeFe_2O_4$. As shown in Fig. 3c, completely different metal–oxygen covalencies are obtained depending on whether the cation's substitution site is tetrahedral or octahedral, which suggests that controlling the substitution site is a practicable strategy in manipulating the covalency in spinel. Among the screened candidates, the Max($D_T$, $D_O$) values predicted by the covalency competition model for spinels $[Mn]_T[Cu_{0.5}Mn_{1.5}]_OO_4$, $[Mn]_T[Al_{0.5}Mn_{1.5}]_OO_4$ and $[Mn]_T[Zn_{0.5}Mn_{1.5}]_OO_4$ are close to the optimal value, estimating good OER activity. However, as copper and zinc generally exhibit a +2 valence state in oxides and situate in the tetrahedral sites[20,28], difficulties may arise in synthesizing the matching structure experimentally. By contrast, metal aluminium typically shows +3 valence state and usually takes the octahedral sites in spinel structures[29]. The predicted spinel $[Mn]_T[Al_{0.5}Mn_{1.5}]_OO_4$ should therefore be a promising highly active and experimentally feasible catalyst.

**Synthesis, characterization and OER activity of $[Mn]_T[Al_{0.5}Mn_{1.5}]_OO_4$.** Spinel $Al_{0.5}Mn_{2.5}O_4$ was synthesized and characterized to confirm the OER performance of the as-predicted aluminium substituted $MnMn_2O_4$. As shown in Fig. 4a, energy-dispersive X-ray spectroscopy (EDS) illustrates that manganese and aluminium distribute evenly in the oxide, implying the crystallization of aluminium, manganese and oxygen in spinel $Al_{0.5}Mn_{2.5}O_4$. The high-angle annular dark-field (HAADF) scanning transmission electron microscopy (STEM) image in Fig. 4b shows lattice directions of [001] and [110]. From the bottom-right pattern, it can be obviously seen that each oxygen in the spinel lattice is shared by three octahedral cations and one tetrahedral cation. The X-ray diffraction (XRD) pattern (Fig. 4c) of the as-synthesized oxide indicates a typical tetragonal spinel structure. The observed peaks at around 18.0°, 28.9°, 32.3°, 36.1° and 59.8° correspond to the (101), (112), (103), (211) and (224) lattice planes of $MnMn_2O_4$, respectively (JCPDS PDF#24-0734). When aluminium substitutes for manganese in the $MnMn_2O_4$ lattice, all of the diffraction peaks show a slight rightwards shift, which is a result of the lattice shrinkage caused by the partial replacement of manganese atoms by aluminium with a smaller radius[30]. All of the above results indicate that the structure of $Al_{0.5}Mn_{2.5}O_4$ remains as a spinel frame.

X-ray absorption near-edge spectroscopy (XANES) data for manganese K- and $L_{2,3}$-edges were collected to probe the valence and occupation state of manganese in the spinel oxide[31]. The manganese K-edge XANES (Supplementary Fig. 7) shows that the manganese valence state of $Al_{0.5}Mn_{2.5}O_4$ is between that of MnO and $Mn_3O_4$, which qualitatively implies that aluminium mainly locates in the octahedral sites, as $Mn^{2+}$ prefers to occupy the tetrahedral interstices while $Mn^{3+}$ tends to occupy the octahedral interstices[10]. We have performed the $L_{2,3}$-edge X-ray absorption spectrum (XAS) linear-combination fitting to quantitatively obtain the manganese occupation in $Al_{0.5}Mn_{2.5}O_4$, using MnO and $Mn_2O_3$ as reference samples (Fig. 4d)[32]. The fitting results suggest that almost all of the aluminium atoms reside in the octahedral sites, implying a chemical formula of $[Mn]_T[Al_{0.5}Mn_{1.5}]_OO_4$ for spinel $Al_{0.5}Mn_{2.5}O_4$ (more details of the manganese occupation fitting can be found in Methods, Supplementary Table 8 and Supplementary Fig. 8). Subsequent electrochemical measurements were performed within a potential window of ~1.0–1.8 V (versus RHE) in 0.1 M KOH, with the catalytic activities being normalized by the surface area of oxides to reflect the intrinsic activity (Fig. 4e)[33,34]. The surface area of the as-synthesized spinel was determined by Brunauer–Emmett–Teller (BET) measurements, which is considered rational for measuring metal oxide catalysts[34–36]. As shown in Fig. 4e, the potential of the OER on spinel $[Mn]_T[Al_{0.5}Mn_{1.5}]_OO_4$ is characterized to be 1.47 V (versus RHE) at a current density of 25 μA $cm_{ox}^{-2}$; that is, an overpotential of 240 mV. Spinel $[Mn]_T[Al_{0.5}Mn_{1.5}]_OO_4$ locates at the summit of the established volcano-shaped plot, indicating remarkable

activity for OER (insert box in Fig. 4e). It is worth noting that the inductively coupled plasma (ICP; Supplementary Table 11) and line scan (Supplementary Fig. 10) results suggest that aluminium is partially leached out into the solution; however, a high-resolution transmission electron microscopy study of the samples before and after long-time OER cycling (Supplementary Fig. 10) revealed that no surface reconstructions to amorphous or hydroxides structures occur, indicating that the exhibited activity is still attributed to the oxide in the spinel frame. Furthermore, spinel $[Mn]_T[Al_{0.5}Mn_{1.5}]_OO_4$ with partial aluminium vacancies are also remarkable OER catalysts, as their predicted Max($D_T$, $D_O$) are close to the optimal value of 3 eV (Supplementary Fig. 11). The stability tests (over 1,000 cycles and 12 h chronoamperometry) demonstrate a good durability of the as-synthesized spinel under the operating condition (Supplementary Fig. 12). The comparison between the intrinsic OER activity of the as-synthesized $[Mn]_T[Al_{0.5}Mn_{1.5}]_OO_4$ with that of the state-of-the-art catalysts[37–40] was performed thereafter (Fig. 4f), further confirming the high intrinsic activity of spinel $[Mn]_T[Al_{0.5}Mn_{1.5}]_OO_4$. The TOF is used to represent the intrinsic activity, which was calculated by assuming that the surface metal atoms are active sites. As illustrated, the TOF calculated for $Ni_{0.55}Fe_{0.45}OOH$ is 1.35 $s^{-1}$, which is the best reported OER catalyst in 0.1 M KOH so far[40]. For spinel $[Mn]_T[Al_{0.5}Mn_{1.5}]_OO_4$, the calculated TOF is 0.45 $s^{-1}$, indicating slightly poorer activity than the benchmark $Ni_{0.55}Fe_{0.45}OOH$; however, its TOF is higher than many of the other reference catalysts, including $IrO_2$ (ref. [37]), $NiFe(OH)_2$, $RuO_2$ (ref. [38]) and the perovskite $Ba_{0.5}Sr_{0.5}Co_{0.8}Fe_{0.2}O_{3-\delta}$ (ref. [38]). Finally, the free energy diagram of OER on tetrahedral manganese was calculated. As shown in Fig. 4g, the overpotential on spinel $[Mn]_T[Al_{0.5}Mn_{1.5}]_OO_4$ mainly results from the inadequate adsorption energy of *OH and *OOH, which stay above the level of an ideal catalyst[41]. To initiate the reaction, a 1.474 eV uphill free energy needs to be surmounted to make the rate-determining step of *OH to *O (*OH + $OH^-$ → *O + $H_2O$) a thermally neutral process, estimating a 1.474 V (versus RHE) reaction potential. The superior OER activity of the as-predicted $[Mn]_T[Al_{0.5}Mn_{1.5}]_OO_4$ is therefore experimentally confirmed.

## Conclusions

In summary, we employ both computational and experimental approaches to describe how the OER mechanism and activity on spinel oxides can be associated with their bulk electronic structures. The OER mechanism on spinel is demonstrated to be simultaneously determined by the oxygen p band centre and the relative reactivity between the oxygen p and metal d bands. The OER activity originates from the covalency competition between tetrahedral and octahedral cations for overlapping with oxygen p orbitals ($M_T$–$M_O$ competition), which results in an asymmetric $M_O$–O–$M_T$ backbone and regulates the exposure of active catalysis sites. The ability of $M_O$–O–$M_T$ break is found to volcanically relate to OER activity. A machine-learning enabled mathematical approach was further developed for ultrafast covalency competition screening. The established covalency competition model provides the covalency competition result in spinel with the mean absolute error of only 0.05 eV. The approach predicted spinel $[Mn]_T[Al_{0.5}Mn_{1.5}]_OO_4$ to be an outstanding electrocatalyst for OER. Subsequent experiments validated the OER activity of the as-designed spinel, which exhibits only 240 mV (versus RHE) overpotential at 25 μA $cm_{ox}^{-2}$. These findings provide comprehensive understanding of oxygen electrocatalysis by spinel oxides and present the related design concepts. Besides, it is worth noting that the covalency competition theory is a universal structure–property relation that is applicable to all spinel families, and it best describes those thermodynamically stable spinels that keep the $AB_2O_4$ frame under OER conditions. For those undergoing surface reconstruction to amorphous or hydroxide structures, evaluations on the bulk features that induce the surface reconstruction and the thermochemistry of the reconstructed surface are also
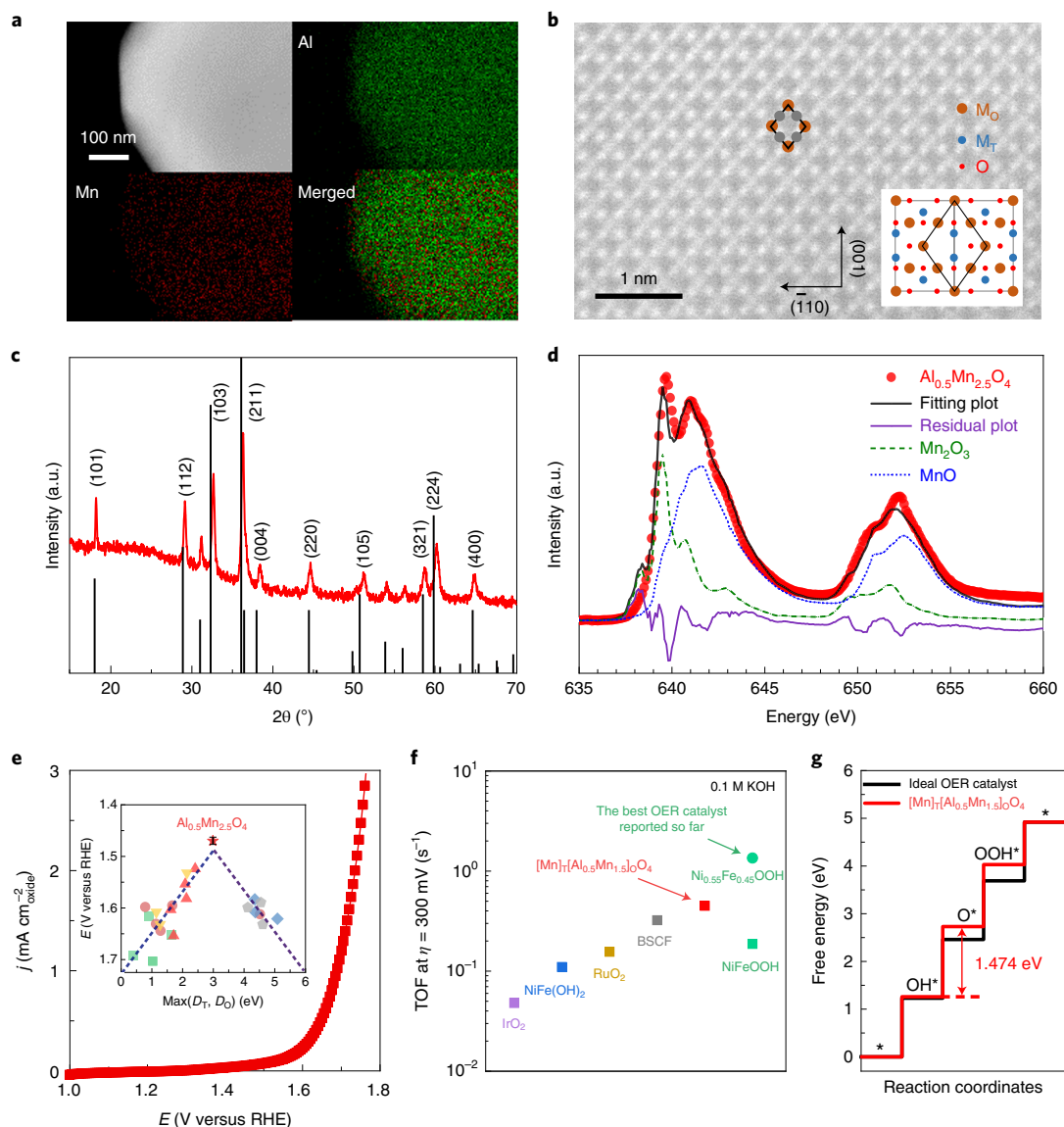
**Fig. 4 | Experimental analysis of the synthesized spinel $Al_{0.5}Mn_{2.5}O_4$. a**, An EDS elemental mapping of spinel $Al_{0.5}Mn_{2.5}O_4$. **b**, A HAADF STEM image of the as-synthesized $Al_{0.5}Mn_{2.5}O_4$. **c**, The XRD pattern of the as-synthesized spinel $Al_{0.5}Mn_{2.5}O_4$. **d**, A linear-combination fitting for the manganese $L_{2,3}$-edge XAS of the as-synthesized $Al_{0.5}Mn_{2.5}O_4$, using MnO and $Mn_2O_3$ as reference samples. **e**, iR-corrected linear sweep voltammetry (LSV) curves of the as-synthesized $Al_{0.5}Mn_{2.5}O_4$ oxide. The inset illustrates the location of $Al_{0.5}Mn_{2.5}O_4$ in the constructed volcano plot. The error bar was obtained by repeating the electrochemical test three times. $j$, the current density normalized by Brunauer–Emmett–Teller (BET) surface area. The raw LSV data are shown in Supplementary Fig. 9. **f**, The turnover frequency (TOF) of the as-synthesized $Al_{0.5}Mn_{2.5}O_4$ and other reference OER catalysts in 0.1 M KOH at an overpotential, $\eta$, of 300 mV. The red square is the TOF of $Al_{0.5}Mn_{2.5}O_4$. The purple square is the TOF of $IrO_2$, which was calculated on the basis of data from work by Stoerzinger and colleagues[37]. The blue square is the TOF of $NiFe(OH)_2$, which was synthesized in this work. The TOF values of $RuO_2$ (yellow square) and BSCF (grey square) are directly taken from work by Hong and co-workers[38]. The green data represent the TOFs of $Ni_aFe_{1-a}OOH$,: the green square is the average performance of NiFeOOH from the work by Diaz-Morales and co-workers[39], whereas the upper green circle is the TOF of $Ni_{0.55}Fe_{0.45}OOH$ from the work by Görlin and colleagues[40], which is the best OER catalyst in 0.1 M KOH reported so far. The synthesis, characterizations and OER measurements of $NiFe(OH)_2$ are detailed in the Methods. The TOF-calculation procedures are detailed in equations (3–14). **g**, A DFT-calculated OER free energy diagram on the most close-packed surface of $[Mn]_T[Al_{0.5}Mn_{1.5}]_OO_4$ oxide. Tetrahedral manganese is considered to be the active site. The pathway on an ideal catalyst is also shown for reference.

essential to give a more characteristic description. The mathematical model established here may be extendable to other applications, in which high-performance spinel oxides are needed.

## Methods

**DFT calculations.** All of the spin-polarized DFT calculations were performed with the Vienna ab initio simulation package[42,43], employing the projector augmented-wave[44] model. The exchange and correlation effects were described by Perdew–burke–Ernzerhof[45] functional, under the generalized gradient approximation approach. The Hubbard $U$ corrections were adopted where transition metals are contained, using the model proposed by Dudarev and colleagues[46]. The $U_{eff}$ ($U_{eff}$ = Coulomb ($U$) – exchange ($J$)) values of each transition metal are summarized in Supplementary Table 9. The cutoff energy was set to 450 eV in all cases. The bulk structures of spinel oxides were optimized by using 6×6×6 and 11×11×6 Monkhorst−Pack[47] k-point meshes for the cubic and tetragonal configurations, respectively. After structure optimization, the projected DOS calculations were carried out by using 9×9×9 and 15×15×9

Monkhorst−Pack k-point meshes for cubic and tetragonal spinels, respectively. Of all the calculations, the Brillouin zone was integrated using the tetrahedron method with Blöch corrections[48]. The force and energy convergence tolerance were set to 0.01 eV Å$^{-1}$ and $10^{-5}$ eV, respectively. For spinels with metal substitutes, the guest cations were arranged as randomly as possible inside the spinel lattice. The effective oxygen $p$ and metal $d$ band centres were determined by the weighted average of the $p$ and $d$ band states (both occupied and unoccupied states), respectively, from the computed projected DOS. The atomic coordinates of the spinels for training the covalency competition model are summarized in Supplementary Data 1. The atomic coordinates of the OER intermediates on spinel $[Mn]_T[Al_{0.5}Mn_{1.5}]_OO_4$ are summarized in Supplementary Data 2. The bulk oxygen formation energy of spinel oxides was calculated as the energy difference between the vacant spinel together with an oxygen atom and the intact spinel structure, which was defined as

$$\triangle E_{vacancy-form} = E_{vacant-bulk} + E_{oxygen} - E_{intact-bulk} \qquad (1)$$

where $E_{vacant-bulk}$, $E_{oxygen}$ and $E_{intact-bulk}$ represent the electronic energy of the spinel with one bulk oxygen vacancy, the chemical potential of one oxygen atom referenced to gaseous oxygen molecule and the electronic energy of the intact spinel, respectively[22]. Under this definition, a lower value of bulk oxygen formation energy suggests an easier case for generating an oxygen vacancy.

**Machine-learning approach.** The machine-learning approach was operated on the basis of the DFT-calculated data for fast and accurate covalency competition screening. The machine-learning process was implemented using the open-source Anaconda Distribution (Python 3.7.3, numpy 1.16.2)[49]. The scikit-learn package was used to perform the whole machine-leaning approach. Data training and prediction were carried out under the random forest algorithm, which is an effective learning method for both regression and classification[27,50,51]. We have used the following parameters as input features to describe the structure of spinel $AB_2O_4$: the stoichiometric number of element in tetrahedral and octahedral sites, the electronegativity of each element, the ionic radii of elements in tetrahedral and octahedral sites, the valence electron numbers of each element, the atomic cutoff radius and the band centres in the zinc-blende and rock-salt structures (Supplementary Table 7). The output includes the band centres of oxygen $2p$, $M_O d$, and $M_T d$. The metal–oxygen covalency was then calculated after obtaining these results. The detailed machine-learning procedures in this work are illustrated in Supplementary Figs. 4 and 5. Verification of the machine-learning algorithm was performed by analysing the MAE. The MAE in this work is defined as the average of the absolute errors between the covalency-competition-model-predicted and DFT-calculated Max($D_T$, $D_O$) values. The formula for the MAE is as follows:

$$MAE = \frac{1}{n}\sum_{t=1}^{n}|P_i - C_i| \qquad (2)$$

where $P_i$ is the value predicted by covalency competition model, $C_i$ is the value calculated by DFT and $n$ is the total number of screened spinels.

**Synthesis and characterization of $Al_{0.5}Mn_{2.5}O_4$.** Spinel $Al_{0.5}Mn_{2.5}O_4$ was synthesized through a sol-gel combustion method[52]. All chemicals were used as bought without further purification. In the synthesis process, 5 mmol of $Al(NO_3)_3$ (Sigma-Aldrich) and 25 mmol of $Mn(CH_3COO)_2$ (Sigma-Aldrich) were mixed in diluted nitric acid solution (30 ml deionized water + 5 ml nitric acid) by vigorous stirring; 15 mmol of citric acid (Sigma-Aldrich) was then added into the mixture, acting as a chelating agent. After stirring at 90 °C for 9 h, the mixture solution was converted into viscous gel. The gel was then decomposed in air at 170 °C (the heating rate was set to be 10 °C min$^{-1}$) for 12 h to thoroughly remove the remaining water and ground. After applying a further heat treatment in air at 1,100 °C (with a heating rate of 5 °C min$^{-1}$) for 6 h, phase-pure spinel oxide particles were obtained.

The HAADF-STEM image was obtained on a JEOL ARM200F (JEOL) aberration-corrected transmission electron microscope operated at 200 kV with double-hexapole caesium correctors (CEOS GmbH) and a cold-field emission gun. The convergent semiangle of the probe was set to be around 30 mrad. The HAADF-STEM image was collected by using a half-angle range from 68 to 280 mrad. The EDS was carried out on a JEOL JEM-2100 field emission TEM operated at 200 kV. The crystalline phase of the samples was determined by XRD data, which were collected on a Bruker D8 powder diffractometer with copper Kα radiation ($\lambda$ = 0.15418 nm) operated at 45 kV and 40 mA. Thermogravimetric analysis (TGA) was conducted on a TGA TA Instruments Q500 System under air flow (60 ml min$^{-1}$) with a heating rate of 10 °C min$^{-1}$. The BET measurements were performed on an ASAP Tri-star II 3020 physisorption analyser at 77 K.

**XANES.** XANES of manganese K-edge were collected at the X-Ray Absorption Facility for Catalysis Research beamline of the Singapore Synchrotron Light Source[53]. The sample was prepared by compacting the mixture of spinel oxide powders and boron nitride (powder, ~1 μm, 98%, Sigma-Aldrich) into pellets. Data reduction and data analysis were performed with the Demeter 0.9.26 software package[54]. A normalized absorption ranging from ~0.15–1.00 has been chosen to determine the position of edges. The manganese K-edge XANES spectra of the as-synthesized $Al_{0.5}Mn_{2.5}O_4$ and standard samples is shown in Supplementary Fig. 6.

**$L_{2,3}$-edge XAS.** The $L_{2,3}$-edge XAS data were collected at the soft X-ray and ultraviolet beamline of the Singapore Synchrotron Source[55], which is a compact, 700 MeV electron storage ring that produces synchrotron radiation from two superconducting dipoles having a magnetic flux density of 4.5 T, with a ring circumference of 10.8 m. The manganese $L_{2,3}$-edge spectra were fitted by means of a linear-combination analysis, using the spectra of reference manganese oxides for each of the manganese cations; that is, MnO for $Mn^{2+}$ and $Mn_2O_3$ for $Mn^{3+}$. This method has been reported before and proved to provide effective manganese occupation in the spinel structure[32]. We also fitted the manganese occupation of the $Mn_3O_4$ standard sample to test the validation of this fitting approach (Supplementary Fig. 7). The parameters obtained from fitting the manganese $L_{2,3}$-edge XAS are summarized in Supplementary Table 8. The closeness between the obtained $Mn_3O_4$ parameters and the real manganese occupation in $Mn_3O_4$ confirms the effectiveness of this fitting method.

**Electrochemical measurement of OER activities.** The as-synthesized spinel catalyst, acetylene black and Nafion solution were mixed through ultrasonication for 2 h in ethanol to form the uniform catalyst ink; 10 μl of as-prepared ink with final concentrations of 1.8 mg ml$^{-1}$ oxide, 4.2 mg ml$^{-1}$ acetylene black and 1 mg ml$^{-1}$ Nafion were dropped onto the glassy carbon electrode (geometric surface area: 0.196 cm$^2$). Oxygen electrocatalysis experiments were conducted in $O_2$-saturated 0.1 M KOH with a platinum counter electrode and a Hg/HgO reference electrode. The scan rate for LSV and cyclic voltammetry was kept at 10 mV s$^{-1}$. All of the polarization curves were iR-corrected with regards to the ohmic resistance of the solution. The resistance was measured with the electrochemical impedance spectroscopy technique, which was performed using alternating current impedance spectroscopy, with the working electrode biased as a certain potential while the frequency ranged from 100 kHz to 0.01 Hz. The capacitive current was corrected by averaging the forwards and backwards sweeps[56]. The current densities in all of the tests were normalized to the catalyst surface area, which was determined by BET measurements. The overpotential was calculated as the difference between the reaction potential (at 25 μA cm$_{ox}^{-2}$) and the equilibrium potential (1.23 V).

**Synthesis, characterization and OER measurements of $NiFe(OH)_2$ in this work.** The NiFe double hydroxides were prepared by the coprecipitation route, using 0.1 M solutions of $Ni(NO_3)_2$ and $Fe(NO_3)_3$ as precursors. The precipitation was performed at 80 °C; 10 ml water was first adjusted to a pH 9 solution with 0.1 M $Na_2CO_3$. A solution containing 0.1 M $Ni(NO_3)_2$ and 0.1 M $Fe(NO_3)_3$ was then slowly added to mix with the previously prepared solution. The pH was kept approximately constant at nine during the synthesis by simultaneous dropping of 0.1 M $Na_2CO_3$. The addition of the $Ni^{2+}/Fe^{3+}$ solution (30 ml) and $Na_2CO_3$ was completed within 1.5 h, after which the suspension was separated by centrifuge at 5,000 r.p.m. for 5 min. The powders were subsequently dried overnight at 120 °C for two days and finely ground.

The crystalline structure of the samples was measured by XRD data collected on a Bruker D8 powder diffractometer with copper Kα radiation ($\lambda$ = 0.15418 nm) operated at 45 kV and 40 mA. TGA was conducted on a TGA TA Instruments Q500 System under air flow (60 ml min$^{-1}$) with a heating rate of 10 °C min$^{-1}$. EDS was carried out on a FESEM 7600F at 15 kV. The BET measurements were performed on ASAP Tri-star II 3020 physisorption analyser at 77 K. The OER measurement procedure of $NiFe(OH)_2$ was the same as that of spinel $[Mn]_T[Al_{0.5}Mn_{1.5}]_OO_4$.

**TOF calculations of $[Mn]_T[Al_{0.5}Mn_{1.5}]_OO_4$ and $NiFe(OH)_2$ in this work, and $Ni_aFe_{1-a}O_xH_y$, $IrO_2$, $RuO_2$ and BSCF.** The TOFs of these catalysts were calculated using the following equation

$$TOF = \frac{j_{BET} \times A_{oxide}}{4 \times e \times N} = \frac{j_{BET}}{4 \times e \times \rho} \qquad (3)$$

where $j_{BET}$, $A_{oxide}$, $N$, $\rho$ and $e$ represent the BET normalized current density at the overpotential of 300 mV, the surface area of the lattice plane, the number of atoms within the lattice plane, the density of surface metal atoms and the charge of a single electron, respectively.

**$Al_{0.5}Mn_{2.5}O_4$.** To estimate the number of surface manganese atoms, we have used the surface density of atoms within the (111) plane in the unit cell of $[Mn]_T[Al_{0.5}Mn_{1.5}]_OO_4$. The (111) plane is chosen because it is the most close-packed surface of the spinel[57] (with a low surface energy) and has the highest cation density[58] (so that the activity will not be overestimated). Based on the crystallographic data, the number of active manganese atoms ($N_T$, as tetrahedral sites are exposed in this case) and the surface area of the spinel oxide ($A_{oxide}$) can be determined as

$$N_T = 1 \times 0 + \frac{1}{2} \times 2 + \frac{1}{4} \times 2 = 1.5 \text{ atoms} \qquad (4)$$

$$A_{(111)} = \frac{\sqrt{2}a}{2} \times \sqrt{\frac{a^2}{2} + c^2} = \frac{\sqrt{2} \times (5.88 \text{ Å})}{2} \times \sqrt{\frac{(5.88 \text{ Å})^2}{2} + (9.59 \text{ Å})^2}$$
$$= \qquad 4.34 \times 10^{-19} \text{ m}^2 \qquad (5)$$

At an overpotential of 300 mV (with a current density of 0.1 mA $cm_{ox}^{-2}$), the TOF of $[Mn]_T[Al_{0.5}Mn_{1.5}]_OO_4$ should thus be:

$$TOF_T = \frac{j_{BET} \times A_{(111)}}{4 \times e \times N_T} = \frac{(0.1 \times 10^{-3} A\ cm^{-2}) \times (4.34 \times 10^{-19} m^2)}{4 \times (1.60 \times 10^{-19} C) \times 1.5} = 0.45\ s^{-1} \quad (6)$$

**NiFe(OH)₂ in this work.** To find out a rational density of the surface metal atoms (ρ), the value of 12.5 metal atoms per nanometre squared is adopted, which is based on the metal–metal distance of 2.83 Å for $NiFeO_xH_y$, measured in situ under OER conditions[59,60]. The TOF of $NiFe(OH)_2$ was thus calculated as

$$TOF = \frac{0.12\ mA\ cm_{oxide}^{-2}}{4 \times (1.60 \times 10^{-19}\ C) \times (12.5\ nm^{-2})} = 0.15\ s^{-1} \quad (7)$$

**Ni$_a$Fe$_{1-a}$O$_x$H$_y$.** The TOFs of $Ni_aFe_{1-a}O_xH_y$ were calculated based on reported works. The lower level is calculated using the data reported by Diaz-Morales and colleagues[39], where the TOF of the as-synthesized NiFeOOH is calculated as

$$TOF = \frac{0.154\ mA\ cm_{oxide}^{-2}}{4 \times (1.60 \times 10^{-19}\ C) \times (12.5\ nm^{-2})} = 0.19\ s^{-1} \quad (8)$$

The upper level of $Ni_aFe_{1-a}O_xH_y$ is obtained by the work of Mikaela Görlin and co-workers[40], where $a$ equals 0.55. The TOF of $Ni_{0.55}Fe_{0.45}OOH$ was calculated as follows: we first calculated the BET normalized current density

$$j_{BET} = \frac{j_{Geo}}{(\text{Metal loading mass per geometric area}) \times \frac{Mr(Ni_{0.55}Fe_{0.45}OOH)}{Mr(Ni_{0.55}Fe_{0.45})} \times BET} \quad (9)$$

In this formula, the parameter $Mr(x)$ and $j_{BET}$ represent the formula weight of material $x$ and the current density normalized by the BET surface area, respectively; $j_{BET}$ is calculated as

$$j_{BET} = \frac{4.58\ mA\ cm_{Geo}^{-2}}{(10\ \mu g\ cm_{Geo}^{-2}) \times \frac{90.42\ g\ mol^{-1}}{57.41\ g\ mol^{-1}} \times (27\ m^2\ g^{-1})} = 1.08\ mA\ cm_{oxide}^{-2} \quad (10)$$

The TOF was then calculated as

$$TOF = \frac{j_{BET}}{4 \times e \times \rho} = \frac{(1.08\ mA\ cm_{oxide}^{-2})}{4 \times (1.60 \times 10^{-19}\ C) \times (12.5\ nm^{-2})} = 1.35\ s^{-1} \quad (11)$$

In all of the above cases, the value of 12.5 metal atoms per nanometre squared (ρ) is used, which is based on the metal–metal distance of 2.83 Å for $NiFeO_xH_y$, measured in situ under OER conditions[59,60].

**IrO₂.** The TOF of $IrO_2$ is calculated based on the work by Stoerzinger and colleagues[37], where the TOF is calculated as

$$N_{(001)} = 1 \times 0 + \frac{1}{2} \times 0 + \frac{1}{4} \times 4 = 1\ atom \quad (12)$$

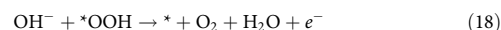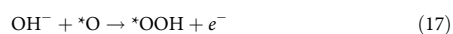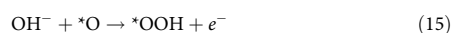$$A_{(001)} = a \times b = (4.545\ \text{Å}) \times (4.545\ \text{Å}) = 2.07 \times 10^{-19} m^2 \quad (13)$$

$$TOF_T = \frac{j_{BET} \times A_{(001)}}{4 \times e \times N_{(001)}} = \frac{(0.015 mA\ cm_{oxide}^{-2}) \times (2.07 \times 10^{-19} m^2)}{4 \times (1.60 \times 10^{-19}\ C) \times 1} = 0.048\ s^{-1} \quad (14)$$

**RuO₂ and BSCF.** The TOF values of $RuO_2$ and BSCF were directly taken from the work by Hong and co-workers[38], in which the values are $0.12\ s^{-1}$ and $0.31\ s^{-1}$, respectively.

**ICP analysis.** ICP analysis was conducted to determine the behaviour of aluminium and manganese leaching in the solutions, and was performed on an Agilent 720 Series ICP-OES with a detection limit of 0.02 ppm. The detailed ICP analysis results are listed in Supplementary Table 11, which indicates that aluminium cations partially leached into the solution. To further investigate the metal–oxygen covalence in aluminium-leached $[Mn]_T[Al_{0.5}Mn_{1.5}]_OO_4$, we have performed predictions for spinel $[Mn]_T[Al_{0.25}Mn_{1.5}]_OO_4$ and $[Mn]_T[Mn_{1.5}]_OO_4$. The results are shown in Supplementary Fig. 11, which indicates spinel $[Mn]_T[Al_{0.5}Mn_{1.5}]_OO_4$ with aluminium vacancy are also excellent catalysts for OER.

**OER free energy calculations.** In alkaline solutions, OER occurs via the following elementary steps:

$$OH^- + *O \rightarrow *OOH + e^- \quad (15)$$

$$OH^- + *OH \rightarrow *O + H_2O + e^- \quad (16)$$

$$OH^- + *O \rightarrow *OOH + e^- \quad (17)$$

$$OH^- + *OOH \rightarrow * + O_2 + H_2O + e^- \quad (18)$$

where * denotes the adsorption sites on the catalyst surface. According to the above four steps, to obtain the pathway of OER, the free energies of *OH, *O and *OOH need to be identified. The computational hydrogen electrode model[61] was used to calculate the free energies of the above-mentioned reaction intermediates, on the basis of which the free energy of an adsorbed species is defined as

$$\triangle G_{ads} = \triangle E_{ads} + \triangle E_{ZPE} - T \triangle S_{ads} \quad (19)$$

where $\Delta E_{ads}$ is the electronic adsorption energy, $\Delta E_{ZPE}$ is the zero-point-energy difference between adsorbed and gaseous species, and $T\Delta S_{ads}$ is the corresponding entropy difference between these two states. The electronic adsorption energy of the three intermediates is defined as

$$\triangle E_{ads} = E_{slab+O_xH_y} - E_{slab} - xE_O - yE_H \quad (20)$$

where $E_{slab+O_xH_y}$, $E_{slab}$, $E_O$ and $E_H$ are the total electronic energy of the adsorption system, the clean slab, and the energies of oxygen and hydrogen atom, respectively. The energy of the oxygen and hydrogen atoms are referenced to $(H_2O – H_2)$ and $1/2\ H_2$, respectively. Using this approach, the OER binding energy volcano and the free energy diagram have been successfully cited[61,62]. The corrections of the zero-point energy and entropy of the OER intermediates are summarized in Supplementary Table 10.

## Data availability
The data supporting the findings of this study are available within the article and its Supplementary Information. Additional data are available from the corresponding authors on reasonable request.

## Code availability
The machine-learning codes for making the covalency competition prediction are available at http://github.com/NTUyuanmiao/Covalency_Competition_Dominates_the_Water_Oxidation_Structure-Activity_Relationship_on_Spinel_Oxides.

## References
1. Armstrong, R. C. et al. The frontiers of energy. *Nat. Energy* **1**, 15020 (2016).
2. Lewis, N. S. & Nocera, D. G. Powering the planet: chemical challenges in solar energy utilization. *Proc. Natl Acad. Sci. USA* **103**, 15729–15735 (2006).
3. Staffell, I. et al. The role of hydrogen and fuel cells in the global energy system. *Energy Environ. Sci.* **12**, 463–491 (2019).
4. Dau, H. et al. The mechanism of water oxidation: from electrolysis via homogeneous to biological catalysis. *ChemCatChem* **2**, 724–761 (2010).
5. Lee, Y., Suntivich, J., May, K. J., Perry, E. E. & Shao-Horn, Y. Synthesis and activities of rutile $IrO_2$ and $RuO_2$ nanoparticles for oxygen evolution in acid and alkaline solutions. *J. Phys. Chem. Lett.* **3**, 399–404 (2012).
6. Seitz, L. C. et al. A highly active and stable $IrO_x/SrIrO_3$ catalyst for the oxygen evolution reaction. *Science* **353**, 1011–1014 (2016).
7. Reier, T., Oezaslan, M. & Strasser, P. Electrocatalytic oxygen evolution reaction (OER) on Ru, Ir, and Pt catalysts: a comparative study of nanoparticles and bulk materials. *ACS Catal.* **2**, 1765–1772 (2012).
8. Yang, L. et al. Efficient oxygen evolution electrocatalysis in acid by a perovskite with face-sharing $IrO_6$ octahedral dimers. *Nat. Commun.* **9**, 5236 (2018).
9. Li, H. et al. Metal–oxygen hybridization determined activity in spinel-based oxygen evolution catalysts: a case study of $ZnFe_{2-x}Cr_xO_4$. *Chem. Mater.* **30**, 6839–6848 (2018).
10. Zhao, Q., Yan, Z., Chen, C. & Chen, J. Spinels: controlled preparation, oxygen reduction/evolution reaction application, and beyond. *Chem. Rev.* **117**, 10121–10211 (2017).
11. Chen, J. Y., Miller, J. T., Gerken, J. B. & Stahl, S. S. Inverse spinel $NiFeAlO_4$ as a highly active oxygen evolution electrocatalyst: promotion of activity by a redox-inert metal ion. *Energy Environ. Sci.* **7**, 1382–1386 (2014).
12. Zhou, Y. et al. Enlarged Co–O covalency in octahedral sites leading to highly efficient spinel oxides for oxygen evolution reaction. *Adv. Mater.* **30**, 1802912 (2018).
13. Duan, Y. et al. Mastering surface reconstruction of metastable spinel oxides for better water oxidation. *Adv. Mater.* **31**, 1807898 (2019).
14. Grimaud, A. et al. Double perovskites as a family of highly active catalysts for oxygen evolution in alkaline solution. *Nat. Commun.* **4**, 2439 (2013).
15. Grimaud, A. et al. Activating lattice oxygen redox reactions in metal oxides to catalyse oxygen evolution. *Nat. Chem.* **9**, 457–465 (2017).
16. Yang, C. & Grimaud, A. Factors controlling the redox activity of oxygen in perovskites: from theory to application for catalytic reactions. *Catalysts* **7**, 149 (2017).

17. Goodenough, J. B. & Loeb, A. L. Theory of ionic ordering, crystal distortion, and magnetic exchange due to covalent forces in spinels. *Phys. Rev.* **98**, 391–408 (1955).

18. Rong, X., Parolin, J. & Kolpak, A. M. A fundamental relationship between reaction mechanism and stability in metal oxide catalysts for oxygen evolution. *ACS Catal.* **6**, 1153–1158 (2016).

19. Zhou, Y. et al. Superexchange effects on oxygen reduction activity of edge-sharing $[Co_xMn_{1-x}O_6]$ octahedra in spinel oxide. *Adv. Mater.* **30**, 1705407 (2018).

20. Wei, C. et al. Cations in octahedral sites: a descriptor for oxygen electrocatalysis on transition-metal spinels. *Adv. Mater.* **29**, 1606800 (2017).

21. Seh, Z. W. et al. Combining theory and experiment in electrocatalysis: insights into materials design. *Science* **355**, eaad4998 (2017).

22. Lee, Y.-L., Kleis, J., Rossmeisl, J., Shao-Horn, Y. & Morgan, D. Prediction of solid oxide fuel cell cathode activity with first-principles descriptors. *Energy Environ. Sci.* **4**, 3966–3970 (2011).

23. Suntivich, J., May, K. J., Gasteiger, H. A., Goodenough, J. B. & Shao-Horn, Y. A perovskite oxide optimized for oxygen evolution catalysis from molecular orbital principles. *Science* **334**, 1383–1385 (2011).

24. Suntivich, J., Perry, E. E., Gasteiger, H. A. & Shao-Horn, Y. The influence of the cation on the oxygen reduction and evolution activities of oxide surfaces in alkaline electrolyte. *Electrocatalysis* **4**, 49–55 (2013).

25. Yang, C., Fontaine, O., Tarascon, J. & Grimaud, A. Chemical recognition of active oxygen species on the surface of oxygen evolution reaction electrocatalysts. *Angew. Chem. Int. Ed.* **56**, 8652–8656 (2017).

26. Garcia, A. C., Touzalin, T., Nieuwland, C., Perini, N. & Koper, M. Enhancement of oxygen evolution activity of nickel oxyhydroxide by electrolyte alkali cations. *Angew. Chem. Int. Ed.* **58**, 12999–13003 (2019).

27. Ahneman, D. T., Estrada, J. G., Lin, S., Dreher, S. D. & Doyle, A. G. Predicting reaction performance in C–N cross-coupling using machine learning. *Science* **360**, 186–190 (2018).

28. Gawande, M. B. et al. Cu and Cu-based nanoparticles: synthesis and applications in catalysis. *Chem. Rev.* **116**, 3722–3811 (2016).

29. Sun, S. et al. Shifting oxygen charge towards octahedral metal: a way to promote water oxidation on cobalt spinel oxides. *Angew. Chem.* **131**, 6103–6108 (2019).

30. Dong, R. et al. Enhanced supercapacitor performance of $Mn_3O_4$ nanocrystals by doping transition-metal ions. *ACS Appl. Mater. Inter.* **5**, 9508–9516 (2013).

31. Liao, H. et al. A multisite strategy for enhancing the hydrogen evolution reaction on a nano-Pd surface in alkaline media. *Adv. Energy Mater.* **7**, 1701129 (2017).

32. Laffont, L. & Gibot, P. High resolution electron energy loss spectroscopy of manganese oxides: application to $Mn_3O_4$ nanoparticles. *Mater. Charact.* **61**, 1268–1273 (2010).

33. Wei, C. & Xu, Z. J. The comprehensive understanding of $10\,mA\,cm^{-2}_{geo}$ as an evaluation parameter for electrochemical water splitting. *Small Methods* **2**, 1800168 (2018).

34. Sun, S., Li, H. & Xu, Z. J. Impact of surface area in evaluation of catalyst activity. *Joule* **2**, 1024–1027 (2018).

35. Jung, S., McCrory, C. C., Ferrer, I. M., Peters, J. C. & Jaramillo, T. F. Benchmarking nanoparticulate metal oxide electrocatalysts for the alkaline water oxidation reaction. *J. Mater. Chem. A* **4**, 3068–3076 (2016).

36. Wei, C. et al. Approaches for measuring the surface areas of metal oxide electrocatalysts for determining their intrinsic electrocatalytic activity. *Chem. Soc. Rev.* **48**, 2518–2534 (2019).

37. Stoerzinger, K. A., Qiao, L., Biegalski, M. D. & Shao-Horn, Y. Orientation-dependent oxygen evolution activities of rutile $IrO_2$ and $RuO_2$. *J. Phys. Chem. Lett.* **5**, 1636–1641 (2014).

38. Hong, W. T. et al. Toward the rational design of non-precious transition metal oxides for oxygen electrocatalysis. *Energy Environ. Sci.* **8**, 1404–1427 (2015).

39. Diaz-Morales, O., Ledezma-Yanez, I., Koper, M. & Calle-Vallejo, F. Guidelines for the rational design of Ni-based double hydroxide electrocatalysts for the oxygen evolution reaction. *ACS Catal.* **5**, 5380–5387 (2015).

40. Görlin, M. et al. Tracking catalyst redox states and reaction dynamics in Ni–Fe oxyhydroxide oxygen evolution reaction electrocatalysts: the role of catalyst support and electrolyte pH. *J. Am. Chem. Soc.* **139**, 2070–2082 (2017).

41. Abild-Pedersen, F. et al. Scaling properties of adsorption energies for hydrogen-contaning molecules on transition-metal surfaces. *Phys. Rev. Lett.* **99**, 016105 (2007).

42. Kresse, G. & Furthmüller, J. Efficient iterative schemes for ab initio total-energy calculations using a plane-wave basis set. *Phys. Rev. B* **54**, 11169–11186 (1996).

43. Kresse, G. & Hafner, J. Ab initio molecular-dynamics simulation of the liquid-metal–armorphous-semiconductor transition in germanium. *Phys. Rev. B* **49**, 14251–14269 (1994).

44. Blöchl, P. E. Projector augmented-wave method. *Phys. Rev. B* **50**, 17953–17979 (1994).

45. Perdew, J. P., Burke, K. & Ernzerhof, M. Generalized gradient approximation made simple. *Phys. Rev. Lett.* **77**, 3865–3868 (1996).

46. Dudarev, S., Botton, G., Savrasov, S., Humphreys, C. & Sutton, A. Electron-energy-loss spectra and the structural stability of nickel oxide: an LSDA+U study. *Phys. Rev. B* **57**, 1505–1509 (1998).

47. Monkhorst, H. J. & Pack, J. D. Special points for Brillouin-zone integrations. *Phys. Rev. B* **13**, 5188–5192 (1976).

48. Blöchl, P. E., Jepsen, O. & Andersen, O. K. Improved tetrahedron method for Brillouin-zone integrations. *Phys. Rev. B* **49**, 16223–16233 (1994).

49. Anaconda Software Distribution. Computer software. v.2-2.4.0. (Anaconda, 2016); https://anaconda.com

50. Svetnik, V. et al. Random forest: a classification and regression tool for compound classification and QSAR modeling. *J. Chem. Inf. Comp. Sci.* **43**, 1947–1958 (2003).

51. Jha, D. et al. Elemnet: deep learning the chemistry of materials from only elemental composition. *Sci. Rep.* **8**, 17593 (2018).

52. Islam, M. et al. Study on the electrochemical reaction mechanism of $NiFe_2O_4$ as a high-performance anode for Li-ion batteries. *ACS Appl. Mater. Inter.* **9**, 14833–14843 (2017).

53. Du, Y. et al. XAFCA: a new XAFS beamline for catalysis research. *J. Synchrotron Rad.* **22**, 839–843 (2015).

54. Ravel, B. & Newville, M. ATHENA, ARTEMIS, HEPHAESTUS: data analysis for X-ray absorption spectroscopy using IFEFFIT. *J. Synchrotron Rad.* **12**, 537–541 (2005).

55. Yu, X., Diao, C., Venkatesan, T., Breese, M. & Rusydi, A. A soft X-ray-ultraviolet (SUV) beamline and diffractometer for resonant elastic scattering and ultraviolet-vacuum ultraviolet reflectance at the Singapore synchrotron light source. *Rev. Sci. Instrum.* **89**, 113113 (2018).

56. Wei, C. et al. Recommended practices and benchmark activity for hydrogen and oxygen electrocatalysis in water splitting and fuel cells. *Adv. Mater.* **31**, 1806296 (2019).

57. Mishra, R. K. & Thomas, G. Surface energy of spinel. *J. Appl. Phys.* **48**, 4576–4580 (1977).

58. Farragher, A. Surface vacancies in close packed crystal structures. *Adv. Colloid Interface Sci.* **11**, 3–41 (1979).

59. Roy, C. et al. Impact of nanoparticle size and lattice oxygen on water oxidation on $NiFeO_xH_y$. *Nat. Catal.* **1**, 820 (2018).

60. Friebel, D. et al. Identification of highly active Fe sites in (Ni, Fe)OOH for electrocatalytic water splitting. *J. Am. Chem. Soc.* **137**, 1305–1313 (2015).

61. Nørskov, J. K. et al. Origin of the overpotential for oxygen reduction at a fuel-cell cathode. *J. Phys. Chem. B* **108**, 17886–17892 (2004).

62. Man, I. C. et al. Universality in oxygen evolution electrocatalysis on oxide surfaces. *ChemCatChem* **3**, 1159–1165 (2011).

## Acknowledgements

## Author contributions

Z.J.X. and Y.S. proposed the research. Y.S., H.L. and Z.J.X. designed the experiments. Y.S. conducted DFT modelling and simulations. H.L. established the mathematical approach. H.L., J.W., S.S., B.C. and S.J.H.O. carried out the experiments. S.X., C.D., Y.D., J.W., J.O.W., Y.S. and H.L. conducted XAS characterizations. Y.S. wrote the manuscript. H.L., S.X., Y.D., M.B.H.B., S.L., H.Z. and Z.J.X. performed the analysis and revised the manuscript.

## Competing interests

The authors declare no competing interests.

## Additional information

**Supplementary information** is available for this paper at https://doi.org/10.1038/s41929-020-0465-6.

**Correspondence and requests for materials** should be addressed to Z.J.X.

**Reprints and permissions information** is available at www.nature.com/reprints.

**Publisher's note** Springer Nature remains neutral with regard to jurisdictional claims in published maps and institutional affiliations.